Spatially Co-registered Wide-field Nonlinear Optical Imaging of Living and Complex Biosystems in a Total Internal Reflection Geometry

ARTICLE

Spatially Co-registered Wide-field Nonlinear Optical Imaging of Living and Complex Biosystems in a Total Internal Reflection Geometry

Uvinduni I. Premadasa,[a] Amber N. Bible,[b] Jennifer L. Morrell-Falvey,[b] Benjamin Doughty,*[a] and Ying-Zhong Ma.*[a]

Nonlinear optical microscopy that leverages an objective based total internal reflection (TIR) excitation scheme is an attractive means for rapid, wide-field imaging with enhanced surface sensitivity. Through select combinations of distinct modalities, one can, in principle, access complementary chemical and structural information for various chemical species near interfaces. Here, we report a successful implementation of such a wide-field nonlinear optical microscope system, which combines coherent anti-stokes Raman scattering (CARS), two-photon fluorescence (TPF), second harmonic generation (SHG), and sum frequency generation (SFG) modalities on the same platform. The intense optical fields needed to drive these high order nonlinear optical processes are achieved through the use of femtosecond pulsed light in combination with the intrinsic field confinement induced by TIR over a large field of view. The performance of our multimodal microscope was first assessed through the experimental determination of its chemical fidelity, intensity and polarization dependences, and spatial resolution using a set of well-defined model systems. Subsequently, its unique capabilities were validated through imaging complex biological systems, including *Hydrangea quercifolia* pollen grains and *Pantoea sp*. YR343 bacterial cells. Specifically, the spatial distribution of different molecular groups in the former was visualized via vibrational contrast mechanisms of CARS, whereas co-registered TPF imaging allowed the identification of spatially localized intrinsic fluorophores. We further demonstrate the feasibility of our microscope for wide-field CARS imaging on live cells through independent characterization of cell viability using spatially co-registered TPF imaging. This approach to TIR enabled wide-field imaging is expected to provide new insights into bacterial strains and their interactions with other species in the rhizosphere in a time-resolved and chemically selective manner.

Introduction

A key element to understanding the synergy of plant-microbe communities lies in being able to detect and interpret the flow of metabolites and signaling molecules across the complex and spatially heterogenous biosystem in real space and time. However, probing these communities is challenging not only because the molecular species of interest are typically present in low abundances and buried within a chemically complex matrix, but also because they are spatiotemporally distributed throughout the system. To address these challenges, a gamut of imaging techniques has been, and continue to be, developed to probe the localization of molecular species with ever increasing fidelity. Of these techniques, nonlinear optical approaches have gained widespread adoption as they open an avenue to probe molecular processes *in vivo* nondestructively, noninvasively, and without the inclusion of extrinsic molecular probes.[1] Amongst the many nonlinear optical methods, two-photon

fluorescence (TPF), second harmonic generation (SHG), and coherent anti-Stokes Raman scattering (CARS) are the most widely utilized tools for probing biological systems. For example, TPF has been extensively used in imaging biological systems via intrinsic fluorescence or, more commonly, through extrinsic labeling. In TPF, two incident photons are simultaneously absorbed to create an electronic excited state from which relaxation back to the ground state results in the emission of Stokes shifted fluorescence photons with higher energy than either of the incident photons.[2, 3] Similarly, SHG and sum-frequency generation (SFG) are second-order nonlinear optical processes where the incident laser fields drive a coherent second order polarization that emits light with energy exactly equal to the sum of the incident laser frequencies.[1, 2, 4] Furthermore, due to symmetry arguments, SHG and SFG processes are sensitive probes for non-centrosymmetric structures such as membranes and chiral assemblies.[5-7] In contrast, CARS microscopy allows for vibrationally selective imaging. CARS is a nonlinear four-wave mixing phenomenon where, traditionally, a pump pulse at a frequency ω_p and a Stokes pulse at ω_s are tightly focused into a sample.[8, 9] When the frequency difference of these pulses matches the frequency of a Raman active molecular vibration, a strong anti-Stokes signal arises in a phase-matched direction. As such, chemical

a. *Chemical Sciences Division, Oak Ridge National Laboratory, Oak Ridge, Tennessee 37831, United States.*
b. *Biosciences Division, Oak Ridge National Laboratory, Oak Ridge, Tennessee 37831, United States.*
* Corresponding authors: doughtybl@ornl.gov and may1@ornl.gov

contrast is derived by mapping the CARS response while scanning incident laser frequencies or the timing between incident laser pulses. Combining these and other nonlinear optical modalities offer the advantage of obtaining complementary chemical and structural information simultaneously by judicious selection of spectral filters, laser pulse timings, and incident laser polarization.[2, 10]

Multimodal nonlinear optical microscopy has been explored in biomedical imaging applications for several decades now. For instance, incorporation of multiple nonlinear optical modalities on a single platform has enabled CARS imaging of myelin sheath, SFG or SHG imaging of astrocyte processes and microtubules, and TPF imaging of other important biological components (e.g., calcium activity).[2, 11] By combining CARS with TPF imaging, the interaction of lipid droplets with mitochondria was studied using fluorescent probes in adrenal cortical cells.[12] Pioneering work by many researchers in the field of biological imaging has allowed the investigation of a broad range of biological questions concerning lipid metabolism, cancer development, cardiovascular diseases, and skin biology. For example, a study carried out by Potma and co-workers provided insights into metabolic processes, unveiling links between cancer metastasis and lipid metabolism, cellular redox state, and the extracellular matrix.[13] Min and colleagues developed strategies to image metabolites in cells by coupling stimulated Raman-scattering microscopy with vibrational tags. They monitored processes such as protein synthesis, drug delivery in animal tissues, and lipid metabolic processes which are important for functions taking place in healthy and diseased tissues.[14] The work by Cheng and co-workers[15] was able to characterize metabolic syndrome-induced cardiovascular plaques through multimodal nonlinear optical imaging of arterial tissues of Ossabaw swine. This work showed the potential application of such a multimodal nonlinear optical imaging tool in the diagnosis of atherosclerotic plaque as well as the design of individualized drug therapy based on plaque composition. While powerful, a vast majority of the multimodal nonlinear bioimaging studies reported in the literature leverage a conventional excitation scheme using tightly focused light, which is a prerequisite to provide sufficiently high excitation fields necessary for generating nonlinear optical phenomena. Typically, the images collected in a focused beam geometry are of excellent quality but are not suitable for isolating processes occurring near an interface or collecting entire images in a single exposure, which is of importance for understanding biofilms and related processes that evolve in space and time.

To address these limitations, wide-field microscopy approaches have been explored as a promising alternative to point scanning methods.[16-19] For instance, a study by Ritsch-Marte and co-workers employed a wide-field approach for CARS microscopy and recognized its potential in applications where faster imaging and higher spectral resolution are more vital than image resolution.[16] Furthermore, to ensure the limits of light exposure for maintaining the viability of living specimens/cells are met, such a wide-field platform can be either epi-illuminated or illuminated via a TIR geometry. The latter selectively illuminates interfacial species via an exponentially decaying evanescent electromagnetic field with a penetration depth smaller than the wavelength of the incident light.[20, 21] As such, TIR-based microscopies could be a convenient approach to image planar samples/specimens such as plant-microbe systems, biofilms, and interfaces in other complex systems where excessive light exposure is undesirable but the unique capability of such wide-field imaging is advantageous. TIR occurs when light is incident on an interface at an angle that exceeds the critical angle, which depends on the refractive indices of the relevant substrate and sample phases.[20, 21] Excitation with a TIR beam geometry can be achieved with a prism-based configuration or an objective-based approach. The objective-based configuration holds a distinct advantage in the types of samples that can be probed, collection efficiency, and ease of incorporation into existing imaging platforms. These advantages are further accompanied by the potential for convenient live cell imaging with limited requirements for sample preparation, reduced photobleaching, and only minor adjustments required to swap between different imaging modalities through changing filters or adjusting laser time delays. So far, only a limited number of studies have been reported with an objective-based TIR excitation geometry, including TPF microscopy,[22, 23] SHG microscopy,[24] electronic SFG spectroscopy,[24, 25] and our recent report on TIR enabled CARS microscopy,[10] as well as surface-enhanced CARS microscopic study by Potma and coworkers.[17]

Herein the realization of a wide-field multimodal nonlinear optical microscope incorporating CARS, SHG, SFG, and TPF modalities in a convenient objective based TIR excitation geometry is demonstrated. The intense optical fields needed to drive these high order nonlinear optical processes are achieved using femtosecond pulsed light in combination with the intrinsic field confinement (and surface sensitivity) induced by TIR over a large field of view. This approach overcomes the bottlenecks in wide-field nonlinear optical imaging by permitting the use of conventional glass microscope coverslips for acquiring images of biological samples in a range of environments. The unique capabilities of our TIR enabled multimodal microscope are validated by acquiring images from model compounds, plant samples, and live bacterial cells. The development of this multimodal imaging platform is expected to enable future studies on plant roots and microbial colonies in real space and time, which will provide new insights into spatiotemporal microbial-plant rhizosphere interactions.

Instrumental Design

The optical layout for our custom-built TIR enabled microscope is shown in Figure 1. In comparison to previously reported wide-field nonlinear optical microscopic platforms,[16, 18, 26, 27] our system uses a rather simple excitation geometry and consists of commonly available optical components, and hence can be easily implemented on existing microscopes.

Specifically, the light source was a mode-locked femtosecond Ti: Sapphire laser (Tsunami, Spectra Physics), which produced ~50 fs pulses centered at ~809 nm at a repetition rate of 82 MHz. The output of the laser was split into two beams using a thin

ARTICLE
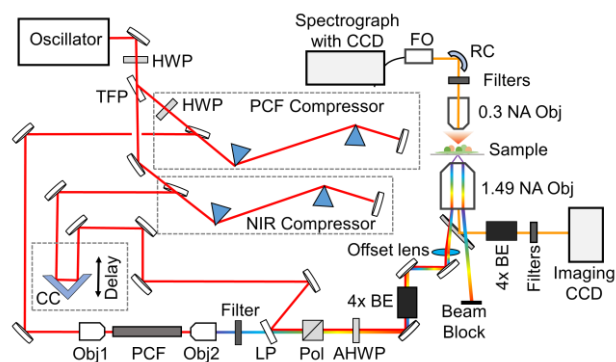
Figure 1. Schematic of TIR enabled wide-field multimodal microscope. HWP: half-wave plate; AHWP: achromatic half-wave plate; TFP: thin-film polarizer; CC- corner cube; PCF: photonic crystal fiber for supercontinuum generation; Obj1 and Obj2: objectives for focusing and collimating the input/output light from the PCF, respectively; LP: long-pass filter; Pol: polarizer; BE: beam expander; RC: reflective fiber collimator; FO: fiber optic bundle.

film polarizer. The power ratio between the two beams was varied using a preceding half-waveplate. The more intense portion of the output (pump beam) was passed through a prism compression line (SF10 prisms) and temporally delayed using a stepper motor driven delay stage (UTM150PP1HL, Newport). An additional half-waveplate/polarizer combination was placed into the beam path to precisely control its power at the sample location. In the second arm, the laser pulse was similarly compressed using a second prism pair and attenuated with another half-waveplate/polarizer combination before being focused into a photonic crystal fiber (PCF, SCG-800-CARS, Newport) for supercontinuum generation using an objective (0.40 NA, 20×). The output of the PCF was collimated using another objective (0.45 NA, 40×), and spectrally filtered using a long-pass filter (FEL0750, Thorlabs) to select the near-infrared portion of the supercontinuum as the Stokes pulse. The pump and Stokes beams were combined collinearly using an 808 nm long-pass filter (LP02-808RU-25, Semrock), which were then polarization purified and rotated using a polarizer and an achromatic half-waveplate, respectively. After passing through a 4× reflective beam expander (BE04R/M - 4× Thorlabs), the beams were focused using an f = 500 mm lens (AC508-500-A-ML. Thorlabs) onto the back focal plane of an oil-immersion high NA microscope objective (Nikon, 1.49 NA, 100×). The lens was translated along one axis via a micrometer to achieve TIR excitation (offset lens in Figure 1), which resulted in a spatially offset back reflection. With the high NA objective in use, the penetration depth of the system was estimated to be in the range of 100 - 250 nm at the glass coverslip-water interface.

In all cases, samples were deposited on a conventional glass coverslip (#1, Fisher Scientific) and placed on a motorized XYZ stage (MCLS03914 and MCLS03914, Mad City Labs Inc). The signal generated from the sample was imaged in the epi-direction using the same objective for achieving TIR, whereas radiated light in the forward direction was collected with an objective (0.30 NA, 10×, Nikon). For imaging experiments, the collected light was first magnified by a 4× beam expander and then spectrally filtered with a 750 nm short pass dichroic mirror (FF750-SDi02, Semrock) in combination with a second optical

filter mounted on a filter wheel, which was chosen depending on the imaging modality in order to reject residual excitation light. The filtered signal was imaged onto an intensified CCD camera with 1024 × 1024 pixels (PI-MAX 7467-0028, Princeton Instruments). The field of view was determined to be 27.9 μm × 27.9 μm using a test target (R3L1S4P, Thorlabs). The signal in the forward direction was similarly doubly filtered using a combination of short-pass filters (750 nm, 64-322, Edmund Optics) and a 785 nm (BSP01-785R-25, Semrock) to isolate the various signals of interest from the residual excitation beams. The filtered signal was then coupled into a fiber optic bundle consisting of nineteen 200 μm fibers using a reflective fiber collimator (RC08SMA-F01, Thorlabs) and detected by a second CCD camera (PI-MAX 7467-0028, Princeton Instruments) mounted on a spectrograph (Acton SP2300, Princeton Instruments). The ICCD camera was not synchronized to the laser repetition rate. Either a 300 or 600 lines/mm grating was chosen to spectrally resolve the radiated signal depending on the spectral ranges probed.
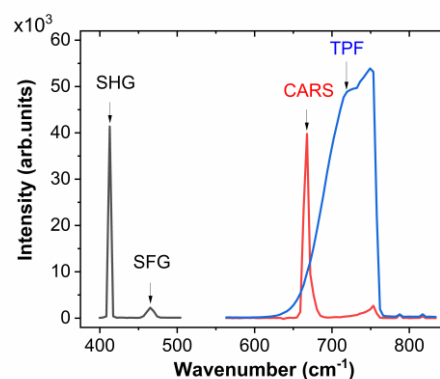
Figure 2: SHG, SFG, and CARS spectra measured from ZnS nanocrystals, along with a TPF spectrum acquired from MG dye.

Microscope Performance

i) Nonlinear Imaging Modalities: Proof of Principle Measurements

Our measurements using test samples below provide a detailed validation of the capabilities and limitations of our TIR enabled multimodal nonlinear optical microscope. This imaging platform is capable of probing CARS, TPF, SHG, and SFG nonlinear optical signals in a wide-field TIR geometry. Each of these nonlinear optical modalities is effectively differentiated based on its characteristic wavelength generated in a specific nonlinear optical process (see Figure 2). For the ~809 nm pump beam and the broadband Stokes beam centered around 1000 nm, the corresponding CARS and SFG signals were observed near ~650 nm and ~450 nm, respectively. Similarly, the SHG signals from the pump beam and Stokes beams can be found near ~404 nm and ~500 nm (data not shown), respectively. Through application of a series of bandpass filters that match spectrally with these wavelength ranges, the nonlinear optical signals

from these modalities can be easily separated and selectively detected using the CCD cameras for imaging and spectral measurements.

First, to evaluate the capabilities of our microscope as a flexible platform for wide-field, multimodal imaging, we prepared a ternary test model sample containing indole-3-acetic acid (IAA), malachite green oxalate dye (MG), and ZnS nanocrystals. IAA is a model biological signaling molecule[28] with a variety of functional groups capable of generating vibrational/chemical contrast. Malachite green is a triarylmethane dye, which not only can emit fluorescence from both its S_1 and S_2 states,[29, 30] but also has been commonly used as an SHG probe in biological systems.[31, 32] Moreover, ZnS nanocrystals are known for

efficient generation of SHG, SFG, and CARS signals due to their intrinsic non-centrosymmetry and high nonlinear susceptibilities. This multi-component system was prepared by first dissolving IAA in methanol, which was directly deposited on the glass coverslip and allowed to dry. Next, a solution of MG dye (1.5 mM in ethanol) was prepared and drop cast onto the same glass coverslip next to the existing IAA film while minimizing its spread. Finally, once both MG and IAA films were dry, ZnS microcrystals were sprinkled on the same coverslip in a third, empty spatial region. The boundaries between these three chemically distinct regions were located via brightfield imaging as shown in Figure 3a, from which a series of nonlinear optical images were collected sequentially in the epi-direction.
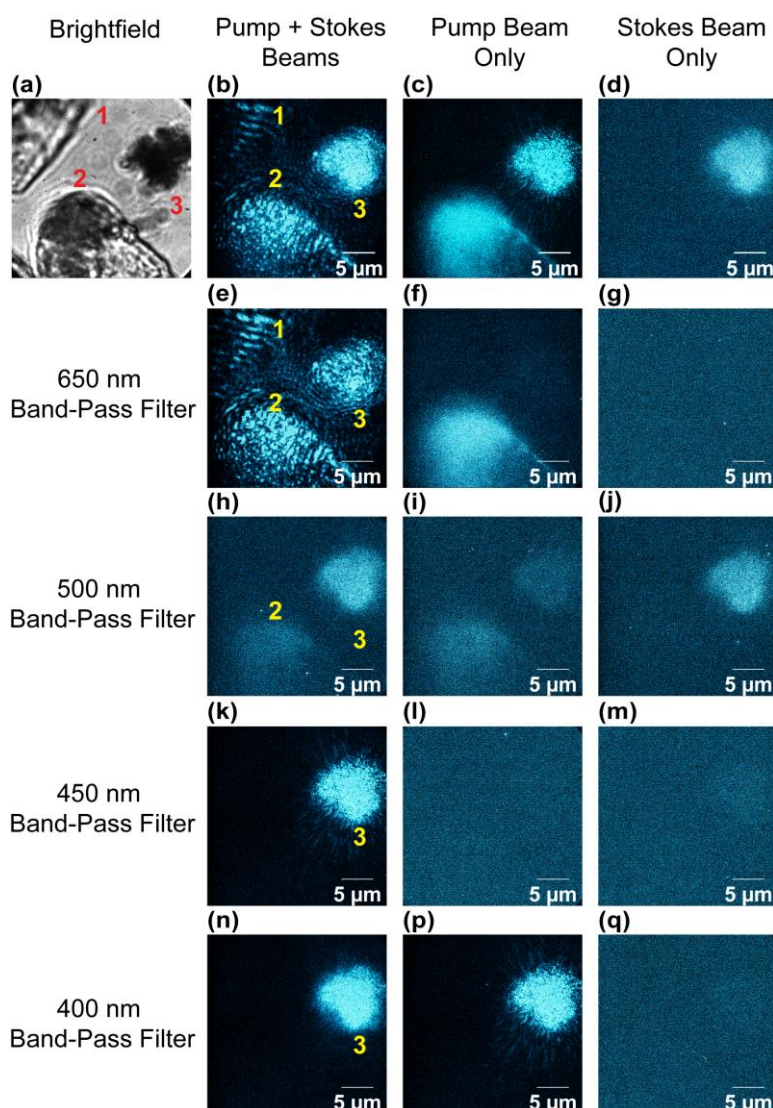
Figure 3. (a) Brightfield and false-colored nonlinear optical images collected at the same sample position from an IAA film (1), MG dye (2), and ZnS nanocrystals (3) on a glass coverslip. The various signals were filtered using either a 725 nm short-pass filter (b-d), or different bandpass filters centered at 650, 500, 450, and 400 nm (e-q), respectively, as indicated in the figure.

All images were background subtracted using a camera exposure for the same duration in the absence of incident light.

For all images shown in Figure 3b-d, the radiated signals were filtered using a 725 nm short-pass filter (#86-103, Edmund

ARTICLE

Optics) to block the residual laser light. The exposure time was set to 30 s to obtain high-quality images without hardware binning. In all cases, the laser power split between the pump and the Stokes beams prior to their respective pulse compression lines was 3.1:1, and the total fluence at the sample stage was ~72 fJ/μm^2.

All these images show clear spatial features that correspond to those observed in the brightfield image (Figure 3a). When both the pump and the Stokes beams were incident on the sample (Figure 3b), a CARS signal was observed in the IAA film (area 1), which was confirmed by its disappearance upon blocking either of the beams (area 1 in Figures 3c,d). The signal from the MG dye (area 2) consists of both CARS and two-photon fluorescence contributions in the presence of both beams as shown in Figure 3b. However, when the Stokes beam was blocked (Figure 3c, area 2), only the two-photon fluorescence signal dominates, along with possibly weak SHG contribution. Furthermore, the nonlinear optical responses from the ZnS nanocrystals (area 3) could contain multiple contributions from CARS, SHG induced by either the pump or the Stokes, respectively, as well as the SFG by the pump and Stokes pulses. In the presence of a single beam, either the pump or the Stokes, only SHG should contribute, leading to reduced overall signal intensity due to the absence of CARS and SFG signals as seen in area 3 in Figure 3c, d. The corresponding variations in area 2 are much more pronounced, manifesting by clear disappearance of either distinct spatial feature as seen in Figure 3c or overall signal as shown in Figure 3d.

To further identify the exact origins of these radiated signals, a set of band-pass filters were utilized to spectrally separate the different nonlinear responses (Figure 3e-3q) based on their characteristic wavelengths. First, the use of a band-pass filter centered at 650 nm with a full-width at half maximum (FWHM) of 40 nm allows observation of the CARS signal from all three components when both the pump and the Stokes beams (Figure 3e) are incident on the sample. This is the only nonlinear signal anticipated here that would generate light in the 650 nm region in the presence of both beams and for all three samples. Second, the two-photon fluorescence from the S_1 state of MG is found at ~670 nm (Figure 3e), which can be separated from the CARS contribution by blocking the Stokes beam while keeping the same 650 nm bandpass filter (Figure 3f). Third, the two-photon fluorescence from the S_2 state of MG is observed at 510 nm, which can be isolated using a 500 nm bandpass filter (84-783, 50 nm FWHM, Edmund Optics) instead as shown in figures 3h and 3i. In addition, the SHG signal from ZnS nanocrystals induced by the Stokes beam (centered at ~1000 nm) can be also isolated with the same 500 nm bandpass filter (Figure 3j). Finally, the SFG and pump derived SHG signals from the ZnS nanocrystal can be separated using a 450 nm band-pass filter (86-653, 25 nm FWHM, Edmund optics) and a 400 nm band-pass filter (FF01-400/40-25, 40 nm FWHM, Semrock), respectively. A straightforward verification of this SFG signal at ~450 nm is to block either of these incident beams and the signal should disappear, which is indeed observed as can be seen in Figure 3l,m. As evident from Figure 3, high-quality, multimodal nonlinear optical images containing
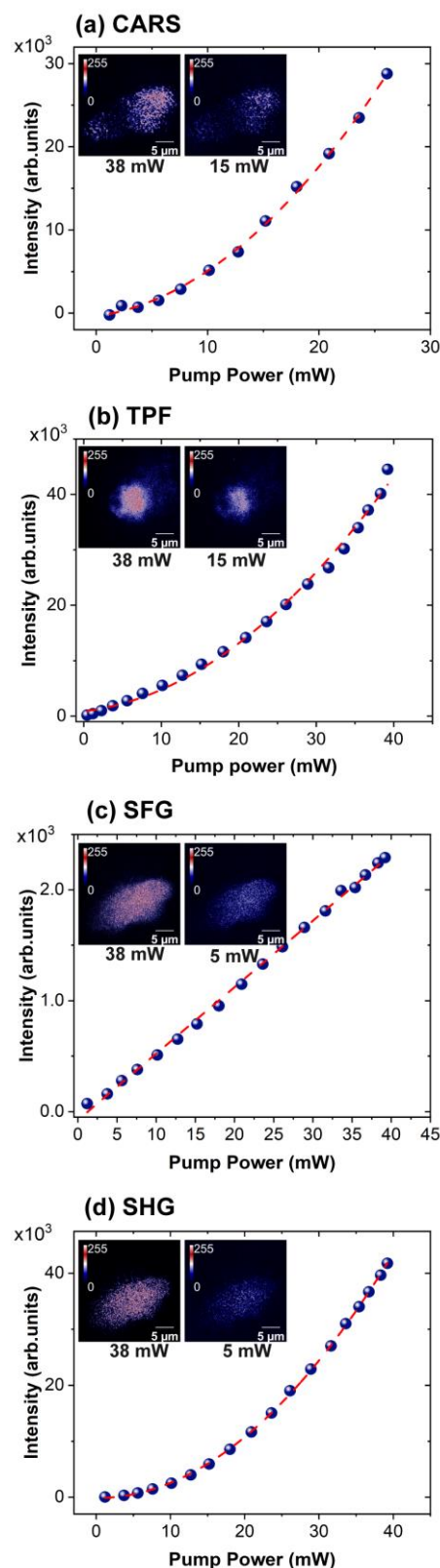
Figure 4. Power laws for the spectral responses of CARS from ZnS (a), TPF from MG dye (b), SFG from ZnS (c), and SHG from ZnS (d) at different pump powers with their corresponding images acquired at two different pump powers (insets).

complementary information can be acquired with modest exposure times. Based on our recent work and these

experiments, such images with reasonable contrast and signal-to-noise ratio (SNR) can be taken using an exposure time as short as 100 ms.

ii) Intensity Dependence

To confirm that the measured signals from these model test compounds were indeed induced by different nonlinear optical processes, we plot the integrated intensities of the spectral responses detected in the forward direction as a function of the input laser power. Here only the pump power was varied, and the Stokes beam power was held constant for the measurements of the CARS, SFG, and SHG spectral responses, whereas the Stokes beam was blocked for corresponding TPF measurements. The incident powers were recorded at the sample position using a microscope slide power meter. As shown in Figure 4a, the integrated intensity of the CARS signal scales quadratically with pump power owing to multiple interactions with the pump field. Such quadratic dependence is also found for both TPF and SHG spectral responses as shown in Figure 4b and d, whereas the corresponding intensity of the SFG signal scales linearly with the pump power as expected. Moreover, acquisition of representative images for these modalities at two different pump powers clearly exhibits a reduced contrast with decreasing power as shown in the insets of Figure 4.

iii) Polarization Dependence

To confirm the detected signals indeed originate from the evanescent fields that extend into the sample from its interface with the coverslip, we leveraged the strong polarization dependence of TIR to examine how these signals vary with the

Figure 5: The bright field and nonlinear optical images acquired with p- and s-polarized input light, respectively, for CARS from IAA (a), TPF from MG dye (b), SFG from ZnS (c), and SHG from ZnS (d).

polarization changes. TIR is achieved using p-polarized light (parallel to the plane of incidence) such that the evanescent field generated will have an elliptical polarization and be confined to a distance of a few 100 nm from the surface. This confinement in the z-direction facilitates notably more intense fields capable of generating nonlinear light-matter interactions.[21, 33] In contrast, if the incident light is s-polarized (perpendicular to the plane of incidence), the TIR condition is not strictly met and consequently, these signals would be correspondingly weaker.[21, 33] To demonstrate this effect, the data in Figure 5 shows the bright field and nonlinear optical images obtained from IAA film, MG dye, and ZnS nanocrystals with s- and p-polarized incident light, respectively. For each of these modalities, the intensity of the nonlinear signal acquired using the s-polarized incident beam is much weaker than that obtained using p-polarized light. This means the signals measured from TIR excitation originate from the species located very near the glass interface, as expected, and that this excitation scheme provides a level of surface specificity through confinement of the optical fields near the interface. The evanescent fields also bolster the field strengths to allow for wide-field excitation and imaging using conventional coverslips for a range of samples.

iv) Spatial Resolution

The spatial resolution of our imaging platform was assessed using the radiated light from particles whose sizes are much smaller than the wavelength of the incident/radiated light, thus can be regarded as point sources. Specifically, a dilute solution of gold nanoparticles of diameter 10 nm was drop cast onto a glass coverslip and the two-photon fluorescence signal emitted was detected at ~ 650 nm (Figure 6a). The only correction made to the presented images was to remove hot pixels. Notably, images from single nanoparticles across the entire field of view are observed, making our microscope suitable for single-particle/single-cell analysis. Single gold nanoparticles were imaged as Airy disks with a two-dimensional (2D) intensity profile corresponding to the point spread function (PSF). Thus, the FWHM value of these 2D intensity profiles can be regarded as the smallest distance that can be resolved in the images. For simplicity, the PSF can be approximated as a 2D Gaussian function[34, 35] described by

$$Z = Z_0 + A\, exp\left\{-\frac{1}{2}\left[\left(\frac{x-x_0}{\sigma_x}\right)^2 + \left(\frac{y-y_0}{\sigma_y}\right)^2\right]\right\} \qquad (1)$$

where Z_0 is a constant related to the background, A is the amplitude, x_0 and y_0 are the coordinates of the center and σ_x and σ_y are widths at 1/e in the x- and y- directions, respectively. The FWHM in the x- and y-directions are given by $2\sigma_{x/y}\sqrt{2\ln 2}$. Figure 6b shows the histograms of the FWHM values determined using the 2D Gaussian function for 50 individual nanoparticles (indicated with yellow arrows) from three different fluorescence images. The average FWHM values in x- and y- directions were (352 ± 19) nm and (350 ± 18) nm, respectively. As a representation, the smoothed intensity profile of an isolated nanoparticle (indicated with a square) is shown in Figure 6c, with the corresponding 2D Gaussian fits
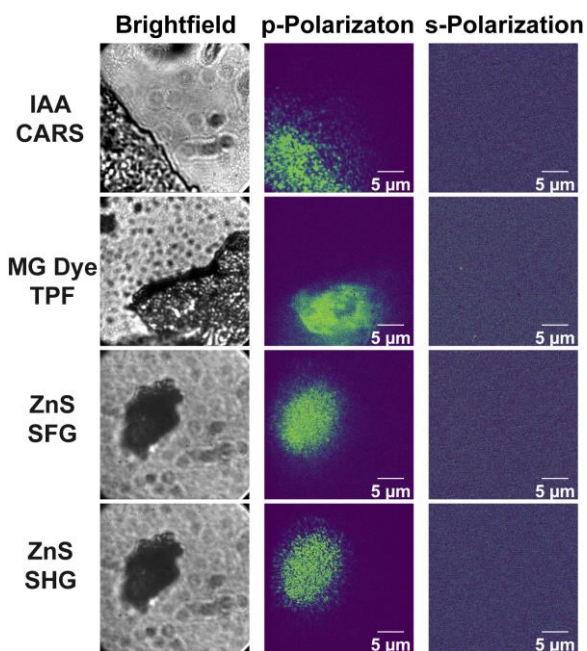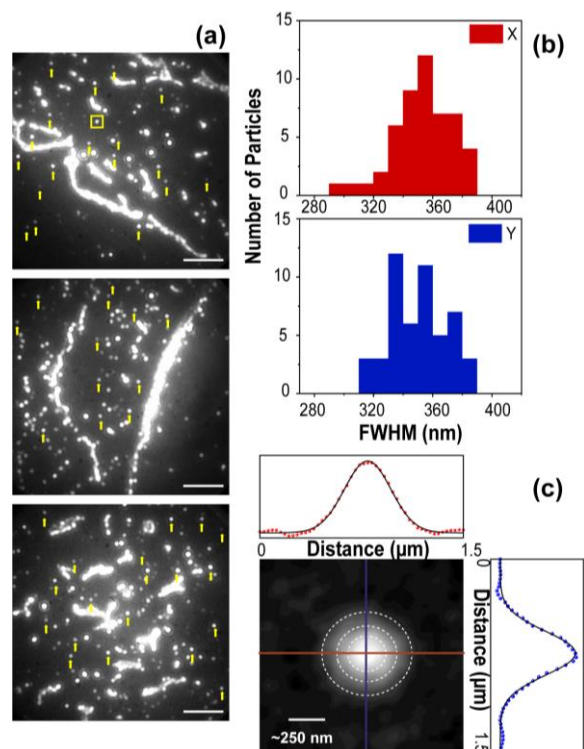
ARTICLE

Figure 6: (a) Two-photon fluorescence images of gold nanoparticles (10 nm) on a glass coverslip (scale bars ~5 μm). (b) Histograms of the FWHM values determined using a 2D Gaussian function for 50 isolated nanoparticles (indicated with yellow arrows). (c) The 2D Gaussian fit and 1D Gaussian fits of the cross-sections (horizontal and vertical) of the fluorescence image of an individual nanoparticle (indicated with a square in the top panel of a).

(white dash lines). The FWHM values determined for the image of this specific isolated nanoparticle in the x- and y- directions are 354 nm and 346 nm, respectively. For comparison, the same isolated nanoparticle image was also fitted separately with the 1D Gaussian function in x- and y- directions, and the resulting FWHM values are 356 nm and 354 nm, respectively. The size determined above is slightly larger than the diffraction limited resolution, which is estimated to be ~225 nm for 670 nm light and the 1.49 NA objective. The deviation in the measured spatial resolution could be due to several reasons such as nanoparticle size distribution, nonideal modulation transfer function of high NA microscope objectives, pixelation errors in the CCD, and the aberration of relay optics.[36] Similarly broadened FWHM of PSF has been observed previously in TIR setups.[36-38] However, the spatial resolution estimated from our experimental determination is still well suited for studying many biological samples such as bacterial cells and similar systems on the micrometer length scales.

v) Chemical Imaging

The chemical imaging capabilities of our multimodal nonlinear optical microscope were validated by measuring the CARS response from an IAA film. The wide spectral range necessary for imaging different molecular resonances is afforded by the spectrally broad (spanning from ~800 nm to ~1330 nm) and temporally chirped Stokes beam (~ 2 ps based on the cross correlation with pump pulse). As a result, probing different

vibrational resonances can be achieved by simply changing the time delay between the spectrally narrow pump pulse and the Stokes pulse.[10] In CARS, the anti-Stokes Raman response arises at $\omega_{as} = 2\omega_p - \omega_s$ when the frequency difference of the pump pulse (ω_p) and the Stokes pulse (ω_s) matches the frequency of a Raman active molecular vibration. By determining the ω_{as} as a function of different delay times, the corresponding Raman shift $\omega_p - \omega_s$ can be obtained in a straightforward manner, since ω_p is known and can be independently measured. This approach is generally known as spectral focusing.[39, 40]

To calibrate the Raman shift vs time delay, time-domain CARS spectral responses in the forward direction as shown in Figure 7(a) were recorded over ~350 different delay times. From the measured spectra, the change of the peak wavelengths of the CARS signals at different time delays represents an indirect measure of the temporal chirp of the Stokes pulse. By plotting these peak wavelengths as a function of time delay and fitting the resulting data to a polynomial function, a universal calibration curve between the Raman shift and time delay is established for our multimodal microscope as shown in Figure
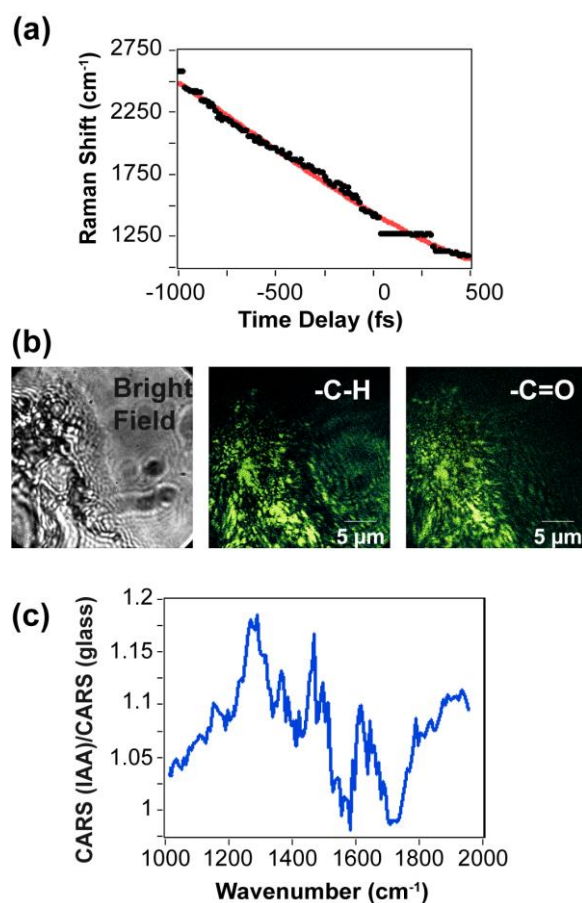
Figure 7: (a) Dependence of the peak CARS frequency vs. time delay measured using a glass coverslip, along with its polynomial fit (red solid line). (b) The brightfield and false-colored CARS images acquired from an IAA film at 2850 cm⁻¹ (-C-H) and 1700 cm⁻¹ (-C=O). (c) The wavelength dependent CARS signal from the IAA film scaled by the signal from a bare coverslip.

7a (solid red line). The wavelength invariance seen from ~50-300 fs delays corresponds to resonant transitions from the cover glass that are commonly found near 1200 cm^{-1}.[41] To demonstrate its unique imaging contrast afforded by simply varying the time delay between the pump and Stokes pulses, and therefore its capability of probing various functional groups, we imaged IAA films in the C-H and C=O vibrational regions. Figure 7b shows the brightfield and CARS images acquired from the IAA film at 2850 cm^{-1} and 1700 cm^{-1}, which are assigned to methylene and carbonyl stretches, respectively. The exposure times for the CARS images acquired at 2850 and 1700 cm^{-1} were 30 and 60 s, respectively. Both CARS images show distinct spatial features dependent on the exact Raman modes being probed, along with nonnegligible non-resonant background. Separating the non-resonant and resonant contributions from a CARS response can be generally realized using established analytical approaches such as Kremer-Kronig and maximum entropy methods,[42, 43] but such an analysis is beyond the scope of this paper. Instead, we verify that the CARS response contains indeed a resonant contribution by plotting a spectral response of the IAA film vs. calibrated Raman shift, which was scaled by the purely non-resonant background measured using a bare coverslip. It should be noted that variations in the NR background with sample position and TIR optimization necessitate collection of a background and signal spectrum at the same position for spectral reconstruction. Figure 7c shows the ratio between the CARS signal from IAA and glass coverslip in the spectral region spanning from 1200 to 1900 cm^{-1}. The rebinned spectrum shows characteristic vibrational signatures of IAA in the range ~1400 - 1450 cm^{-1} and 1600 - 1650 cm^{-1} that can be assigned to C-H bending modes and C=C aromatic stretches, respectively. The vibrational features ~1690 - 1710 cm^{-1} are due to the contribution of C=O stretch and water bending modes. As evident from these measurements and our recent report,[10] our TIR enabled multimodal microscope is capable of generating chemical contrast based on spectral focusing,[39, 40] The typical spectral resolution of our system is ~150 cm^{-1}. As such, this implementation of widefield CARS imaging provides coarse chemical resolution, which could be improved through the use of narrowband and highly chirped pulses at the cost of weaker signals.[44]

Application to Biological Systems

To validate the multimodal capabilities of our nonlinear optical microscope in characterizing biological systems, we performed measurements on the pollen of Oakleaf hydrangea *(Hydrangea quercifolia)* flowers. Pollen grains were chosen because they are complex biological systems involving many biochemical components such as carbohydrates, proteins, lipids, carotenoids, and many other intrinsic fluorophores, making them well suited for multimodal imaging. In addition, morphological information is needed to distinguish pollen grains and has been often used in a taxonomic grouping of their parent plants.[45] So far, only a few reports are available on wide-field multimodal imaging of pollens,[46] and most of the reported
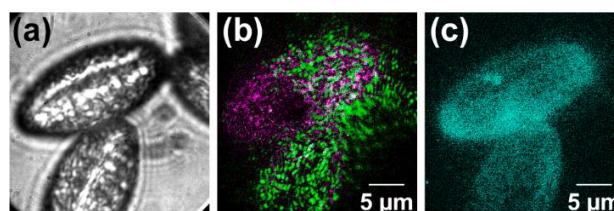
Figure 8: (a) Brightfield, (b) false-colored CARS, and (c) two-photon fluorescence images from Oakleaf hydrangea *(Hydrangea quercifolia)* pollen. The CARS image is a composite of vibrational signatures at 2850 cm^{-1} (green) and 1600 cm^{-1} (purple) showing the distribution of C-H and C=C molecular groups, respectively. The two-photon fluorescence signal was isolated using at 500 nm bandpass filter.

studies are based on either point-scanning methods or a single modality. For instance, fluorescence microscopy has been used to study viability such as the generative nucleus in the pollen tube of lily *(lilium)* pollens.[47] In addition, multiplex CARS microscopy has been used to image lily pollen grains, and the CARS images acquired showed that the structure of the pollen grain reflects their lipid organization.[48] Obviously, a multimodal imaging technique capable of obtaining both chemical and morphological information simultaneously would be more beneficial for palynological studies.

Figure 8 shows the brightfield and the false-colored nonlinear optical images obtained from freshly picked Oakleaf hydrangea flower pollen. No treatments were made to the pollen grains after harvesting from a local tree. Background auto-fluorescence signal from the intrinsic fluorophores observed at ~500-600 nm is likely due to the presence of flavins and flavonoids.[49] The CARS response was separated from this two-photon auto-fluorescence background by subtracting an image acquired in the presence of only the pump beam with the same exposure time. Figure 8b is a composite image of two individual CARS images measured at 2850 cm^{-1} (green) and 1600 cm^{-1} (purple), which probe the spatial distribution of C-H and C=C molecular groups, respectively. Specifically, the vibrational resonance at ~2850 cm^{-1} corresponds to the lipids of the pollen membrane and other aliphatic species.[48] The C=C bonds likely correspond to polyene stretches found in the carotenoids. Notably, this composite image shows clearly spatial heterogeneities, which can arise from differences in chemical localization or through 'shadowing' effects found in the linear analogs of TIR-fluorescence microscopes[50, 51] or from the complex three-dimensional structure of the pollen grains. Since the TIR excitation preferentially probes species near/at the coverslip surface, species located further from the surface do not generate as much signal owing to the exponentially decaying evanescent field. This means that for three-dimensional biological structures that are larger than the evanescent field penetration depth, such as pollen grains, there will be variations in the measured signals that arise from both the proximity of the species to the surface and the respective chemical population. As a result, the intensity of a given signal should encode both the population and the z-position away from the interface between the sample and the coverslip. This further indicates that probing both morphological and chemical

ARTICLE

makeup through variable angle TIR enabled CARS experiments[52] is an exciting and potential avenue for future development.

To assess the feasibility of our multimodal nonlinear optical microscope for imaging live cells, we further performed measurements on fresh cells of the rhizosphere bacterium *Pantoea* sp. YR343. These cells were grown and processed according to our previous reports,[53] and then adhered to a poly-lysine coated glass coverslip and stored in water before experiments. Immediately prior to the experiment, a 1:1 mixture of SYTO9 and propidium iodide (PI) dyes were administered as live/dead stains.[54] SYT09 is a cell permeable DNA dye that fluoresces at ~500 nm, whereas the PI dye emits fluorescence at 620 nm but is cell-impermeable and only stains the DNA of cells with compromised membranes. As such, by spectrally resolving these fluorescence emission signals using proper bandpass filters and imaging the resulting radiated light, we can achieve a live/dead assay to confirm the viability of the cells during CARS imaging. In this experiment the coverslips with dye and adhered cells were mounted in the microscope sample holder and a moist filter paper was kept close to the coverslip to create a humid environment for the cells. Figure 9a shows the brightfield image of the cells before exposure to laser light, and Figure 9b is a composite TPF image collected using different bandpass filters, which shows that most of the cells within the field of view are alive (green) with only a few dead cells (red). Immediately after the completion of this TPF image acquisition, a CARS image was obtained at 2850 cm^{-1} (Figure 9c) with an exposure time of 10 s and a total fluence of ~62 fJ/μm^2 at the sample stage. As shown in Figure 9c, individual cells are clearly visible in the CARS image with a sufficiently high SNR even for such a modest exposure time. The spatial pattern observed in the CARS image is likely due to evanescent field scattering, which is a common observation found in linear TIR microscopic images. Namely, TIR excitation with a single Gaussian laser beam results in shadowing effects due to scattering of the evanescent field by cells which is less apparent at overcritical angle incidence. For linear imaging modalities, spinning the azimuthal angle of TIR incidence with optical devices, or by illuminating in multiple directions in TIR geometry can suppress these shadowing and fringe artifacts.[51] These interferences might be problematic to remove with nonlinear optical modalities with hardware alone due to the coherent nature of the radiated CARS (or SHG/SFG) and the fact one measures the absolute square of the radiated fields and not the fields themselves. Regardless of these artifacts, a clear contrast between the cells and the substrate is found that coincides with the cellular positions seen in the brightfield image (Figure 9a) indicating that while interpretation of small variations in intensity might be prohibitive, larger scale variations are robust and reflective of real spatial heterogeneity. To assess if the laser illumination during the CARS image acquisition has caused substantial cell degradation, we immediately collected a second set of TPF images, which are shown in Figure 9d. We find that some cells do appear to have died as more red spots appear in the image than those seen in Figure 9b, but notably, a majority of the cells still remain intact. The results shown in Figure 9 demonstrate that our wide-field multimodal

microscope developed here is capable of not only directly probing vibrational contrast from *living* systems but also assessing the viability of live cells using the co-registered imaging modalities such as TPF imaging, along with accessing morphological information using brightfield and SHG imaging, etc.

Nonlinear imaging with surface sensitivity can be useful in the study of localization and transport of molecules at or near an interface. For example, this method has a great potential in the area of monitoring biofilm growth and molecular transport within the film vs. in the neighboring bulk phase and thus can enhance the understanding about the interactions of bacterial strains with other species in the rhizosphere in a time-resolved and chemically selective manner.

Conclusions

We have outlined a spatially co-registered multimodal wide-field nonlinear optical microscope based on a TIR beam geometry, which is capable of CARS, TPF, SHG, and SFG imaging. The various modalities offer a powerful means to access complementary chemical and structural information for various species near interfaces. Its performance was thoroughly evaluated through quantification of its spatial resolution, excitation intensity dependence, polarization dependence, and its capabilities for multimodal imaging as well as chemical imaging based on a series of measurements on several model compounds. The unique capabilities of our microscope were further validated by acquiring high-quality images from biological systems including the pollen of Oakleaf hydrangea (*Hydrangea quercifolia*) flowers and live cells of the rhizosphere bacterium *Pantoea sp*. YR343. Our results demonstrate that our wide-field multimodal microscope is capable of not only directly probing vibrational contrast from living systems but also assessing the viability of live cells during image acquisition, along with morphological information using the co-registered imaging modalities. We were able to obtain intrinsically co-registered images reporting on different chemical/structural aspects of the biosystems studied. The results highlight the importance of a spatially co-registered multimodal approach to the microscopy of complex biosystems and how such processes can be driven by leveraging different excitation schemes. In addition, our measurements show the combination of femtosecond light sources with the TIR geometry can provide sufficiently strong excitation fields to drive higher-order optical
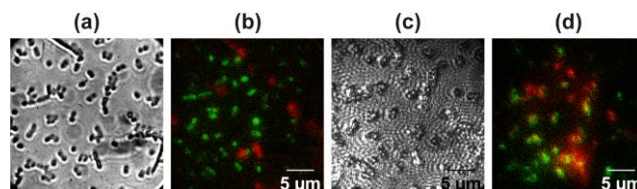
Figure 9: (a) Brightfield and (b,d) composite images of two-photon fluorescence acquired from *Pantoea sp*. YR343 cells stained with SYTO9 and PI dyes before and after CARS imaging, respectively. Two-photon fluorescence emission from SYTO9 (green) and PI (red) are spectrally separated using bandpass filters centered at 500 nm and 650 nm, respectively. (c) CARS image collected at 2850 cm^{-1}.

processes over large excitation areas without specialized sample preparation.

Conflicts of interest

There are no conflicts to declare.

Acknowledgements

References

1. M. J. Blake, B. A. Colon and T. R. Calhoun, *The Journal of Physical Chemistry C*, 2020.
2. S. Yue, M. N. Slipchenko and J. X. Cheng, *Laser & photonics reviews*, 2011, **5**, 496-512.
3. M. Oheim, D. J. Michael, M. Geisbauer, D. Madsen and R. H. Chow, *Advanced drug delivery reviews*, 2006, **58**, 788-808.
4. A. G. Lambert, P. B. Davies and D. J. Neivandt, *Applied Spectroscopy Reviews*, 2005, **40**, 103-145.
5. C. Ding, J. R. W. Ulcickas, F. Deng and G. J. Simpson, *Physical review letters*, 2017, **119**, 193901.
6. A. M. Hanninen, R. C. Prince and E. O. Potma, *IEEE Journal of Selected Topics in Quantum Electronics*, 2018, **25**, 1-11.
7. S. Huang, M. Makarem, S. N. Kiemle, H. Hamedi, M. Sau, D. J. Cosgrove and S. H. Kim, *The Journal of Physical Chemistry B*, 2018, **122**, 5006-5019.
8. A. Khmaladze, J. Jasensky, C. Zhang, X. Han, J. Ding, E. Seeley, X. Liu, G. D. Smith and Z. Chen.
9. A. Khmaladze, J. Jasensky, E. Price, C. Zhang, A. Boughton, X. Han, E. Seeley, X. Liu, M. M. B. Holl and Z. Chen, *Applied spectroscopy*, 2014, **68**, 1116-1122.
10. B. Doughty, U. I. Premadasa, J. F. Cahill, A. B. Webb, J. L. Morrell-Falvey, M. Khalid, S. T. Retterer and Y.-Z. Ma, *Optics Letters*, 2020, **45**, 3087-3090.
11. Y. Fu, W. Sun, Y. Shi, R. Shi and J.-X. Cheng, *PLoS one*, 2009, **4**, e6705.
12. X. Nan, E. O. Potma and X. S. Xie, *Biophysical journal*, 2006, **91**, 728-735.
13. J. Hou, J. Williams, E. L. Botvinick, E. O. Potma and B. J. Tromberg, *Cancer research*, 2018, **78**, 2503-2512.
14. L. Wei, F. Hu, Y. Shen, Z. Chen, Y. Yu, C.-C. Lin, M. C. Wang and W. Min, *Nature methods*, 2014, **11**, 410-412.
15. T. T. Le, I. M. Langohr, M. J. Locker, M. Sturek and J.-X. Cheng, *Journal of biomedical optics*, 2007, **12**, 054007.
16. C. Heinrich, S. Bernet and M. Ritsch-Marte, *Applied physics letters*, 2004, **84**, 816-818.
17. A. Fast, J. P. Kenison, C. D. Syme and E. O. Potma, *Applied optics*, 2016, **55**, 5994-6000.
18. Y. Shen, J. Wang, K. Wang, A. V. Sokolov and M. O. Scully, *APL Photonics*, 2018, **3**, 116104.
19. I. Toytman, D. Simanovskii and D. Palanker, *Optics Express*, 2009, **17**, 7339-7347.
20. D. S. Johnson, J. K. Jaiswal and S. Simon, *Current protocols in cytometry*, 2012, **61**, 12-29.
21. B. A. Colon, M. R. Hassan, A. Saleheen, C. A. Baker and T. R. Calhoun, *The Journal of Physical Chemistry A*, 2020, **124**, 4160-4170.
22. V. G. Bordo, J. Loerke and H. G. Rubahn, *Physical review letters*, 2001, **86**, 1490.
23. B. R. Watson, B. Yang, K. Xiao, Y.-Z. Ma, B. Doughty and T. R. Calhoun, *The Journal of Physical Chemistry Letters*, 2015, **6**, 3283-3288.
24. B. R. Watson, B. Doughty and T. R. Calhoun.
25. B. R. Watson, B. Doughty and T. R. Calhoun, *Nano letters*, 2019, **19**, 6157-6165.
26. C. Heinrich, A. Hofer, A. Ritsch, C. Ciardi, S. Bernet and M. Ritsch-Marte, *Optics Express*, 2008, **16**, 2699-2708.
27. P. Berto, A. Jesacher, C. Roider, S. Monneret, H. Rigneault and M. Ritsch-Marte, *Optics Letters*, 2013, **38**, 709-711.
28. A. N. Bible, S. J. Fletcher, D. A. Pelletier, C. W. Schadt, S. S. Jawdy, D. J. Weston, N. L. Engle, T. Tschaplinski, R. Masyuko and S. Polisetti, *Frontiers in microbiology*, 2016, **7**, 491.
29. M. Yoshizawa, K. Suzuki, A. Kubo and S. Saikan, *Chemical physics letters*, 1998, **290**, 43-48.
30. S. P. Laptenok, K. Addison, I. A. Heisler and S. R. Meech, *Chemical Physics Letters*, 2014, **607**, 43-46.
31. A. Srivastava and K. B. Eisenthal, *Chemical physics letters*, 1998, **292**, 345-351.
32. E. C. Y. Yan and K. B. Eisenthal, *Biophysical journal*, 2000, **79**, 898-903.
33. L. Novotny and B. Hecht, *Principles of nano-optics*, Cambridge university press, 2012.
34. L. Wei, Y. Ma, X. Zhu, J. Xu, Y. Wang, H. Duan and L. Xiao, *Nanoscale*, 2017, **9**, 8747-8755.
35. T. Huang and X.-H. N. Xu, *Nanoscale*, 2011, **3**, 3567-3572.
36. E. Chung, D. Kim, Y. Cui, Y.-H. Kim and P. T. C. So, *Biophysical journal*, 2007, **93**, 1747-1757.
37. E. Chung, D. Kim and P. T. C. So.
38. O. Gliko, G. D. Reddy, B. Anvari, W. E. Brownell and P. Saggau, *Journal of Biomedical Optics*, 2006, **11**, 064013.
39. T. Hellerer, A. M. K. Enejder and A. Zumbusch, *Applied Physics Letters*, 2004, **85**, 25-27.
40. D. Polli, V. Kumar, C. M. Valensise, M. Marangoni and G. Cerullo, *Laser & Photonics Reviews*, 2018, **12**, 1800020.
41. A. K. Yadav and P. Singh, *RSC advances*, 2015, **5**, 67583-67609.
42. Y. Liu, Y. J. Lee and M. T. Cicerone, *Optics letters*, 2009, **34**, 1363-1365.
43. E. M. Vartiainen, *JOSA B*, 1992, **9**, 1209-1214.
44. A. F. Pegoraro, A. Ridsdale, D. J. Moffatt, Y. Jia, J. P. Pezacki and A. Stolow, *Optics express*, 2009, **17**, 2984-2996.
45. M. Sivaguru, L. Mander, G. Fried and S. W. Punyasena, *PloS one*, 2012, **7**, e39129.
46. J. G. Porquez, R. A. Cole, J. T. Tabarangao and A. D. Slepkov, *Biomedical optics express*, 2016, **7**, 4335-4345.
47. A. Sogo and H. Tobe, *Proceedings of the National Academy of Sciences*, 2005, **102**, 8770-8775.

Journal Name

ARTICLE

48. D. S. Choi, J. H. Lee, M.-K. Oh, T. J. Eom, H. S. Kim, H. S. Kang and D.-K. Ko, *Japanese Journal of Applied Physics*, 2011, **50**, 022401.
49. D. J. O'Connor, D. Iacopino, D. A. Healy, D. O'Sullivan and J. R. Sodeau, *Atmospheric Environment*, 2011, **45**, 6451-6458.
50. M. Lei and A. Zumbusch, *Optics letters*, 2010, **35**, 4057-4059.
51. B. Schreiber, K. Elsayad and K. G. Heinze, *Optics Letters*, 2017, **42**, 3880-3883.
52. W. Sun, A. Xu, K. Marchuk, G. Wang and N. Fang, *JALA: Journal of the Association for Laboratory Automation*, 2011, **16**, 255-262.
53. S. Polisetti, A. N. Bible, J. L. Morrell-Falvey and P. W. Bohn, *Analyst*, 2016, **141**, 2175-2182.
54. P. Stiefel, S. Schmidt-Emrich, K. Maniura-Weber and Q. Ren, *BMC microbiology*, 2015, **15**, 36.

1
2
3
4
5
6
7
8
9
10
11
12
13
14
15
16
17
18
19
20
21
22
23
24
25
26
27
28
29
30
31
32
33
34
35
36
37
38
39
40
41
42
43
44
45
46
47
48
49
50
51
52
53
54
55
56
57
58
59
60